Pushing the Limits in Time-of-Flight PET Imaging

P. Lecoq, *Fellow, IEEE*

Abstract—There is an increasing demand for high sensitivity multiparametric medical imaging approaches. High precision time-of-flight positron emission tomography (TOFPET) scanners have a very high potential in this context, providing an improvement in the signal-to-noise ratio of the reconstructed image and the possibility to further increase the already very high sensitivity (at the pico-molar level) of PET scanners. If the present state-of-the art coincidence time resolution of about 500 ps can be improved, it will open the way in particular to a significant reduction of the dose injected to the patient, and consequently, to the possibility to extend the use of PET scans to new categories of patients. This paper will describe the systematic approach followed by a number of researchers worldwide to push the limits of TOFPET imaging to the sub-100 ps level. It will be shown that the possibility to reach 10 ps, although extremely challenging, is not limited by physical barriers and that a number of disruptive technologies are presently being investigated at the level of all the components of the detection chain to gain at least a factor of 10 as compared to the present state-of-the-art.

Index Terms—Clinical imaging systems, new nuclear imaging devices, other emerging materials, photodetector technology, scintillators.

I. INTRODUCTION

POSITRON emission tomography (PET) provides the best quantitative accuracy and molecular sensitivity available today to delineate the contribution of different molecular pathways to metabolic processes in a patient and the way they are affected by diseases. Advances in PET technology result in regular performance improvements and sensitivity increase [1]. The quest for the right prevention and treatment for the right patient at the right time, known as personalized or precision medicine, is at the heart of the healthcare priorities of the 21st century. It is pushing for even more sensitive and precise quantitative and dynamic evaluation of the molecular processes active in some major diseases, such as cancer, cardiovascular and neurodegenerative diseases, diabetes, osteoarthritis, as well as antimicrobial resistance, just to cite a few.

Another motivation for even higher clinical sensitivity is to open the way to a drastic reduction of doses injected to the patient and to generalize molecular imaging procedures to new categories of patients, such as children and pregnant women, including neonatal and event prenatal scans. For pregnant women the international commission on radiological protection recommends the dose to the fetus to be less than 1 mSv [2], to be compared to 8 to 25 mSv whole body PET/CT protocols today.

One possible solution for a significant sensitivity increase by at least one order of magnitude is to extend the angular coverage, presently limited in commercial PET scanners to a few percent only, and to cover the full length of the body with active sensors, so that a much higher fraction of the emitted γ-rays can be detected. This concept of a total body PET scanner has been pushed by the American EXPLORER consortium [3] and has received funding from the NIH Transformative Research Award program for the construction of proof-of-concept prototype in September 2015 [4].

Another approach is to push the limits of time-of-flight PET techniques (TOFPET), motivated by the perspective for a significant improvement in the image signal-to-noise ratio (SNR), resulting in a corresponding clinical sensitivity increase and dose reduction potential according to

$$\text{SNR}_{\text{TOF}}/\text{SNR}_{\text{NONTOF}} = \sqrt{\frac{2D}{c.\text{CTR}}} \tag{1}$$

where

D diameter of the field of view (FOV);
c speed of light in vacuum;
CTR coincidence time resolution.

Presently, the time resolution of commercial whole-body PET cameras is about 500 ps, but a recent measurement of 375 ps has been announced on the Discovery MI PET/CT, using the last generation of silicon photomultiplier (SiPM) photodetectors [5]. For organ specific devices recent developments have shown that 200 ps is within reach (e.g., 227 ps achieved in the FP7 project EndoTOFPET-US at the system level) [6]. If it would be possible to break significantly the 100 ps barrier, not only would the SNR dramatically improve (Fig. 1) but also the possibility to significantly remove artefacts affecting tomographic reconstruction in the case of partial angular coverage will open the field to a larger variety of organ-specific imaging device as well as to imaging-assisted minimally invasive interventions by endoscopy.

Furthermore, if a time resolution of 10 ps could be achieved, this would then lead in a whole body scanner to an uncertainty of only 1.5 mm for a given positron disintegration along the corresponding line of response. Such accuracy is of the order of today's very best small animal or organ specific PET spatial resolution and the time consuming tomographic back-projection or iterative reconstruction algorithms would no longer be needed as true 3-D information would be directly available for each decay event.
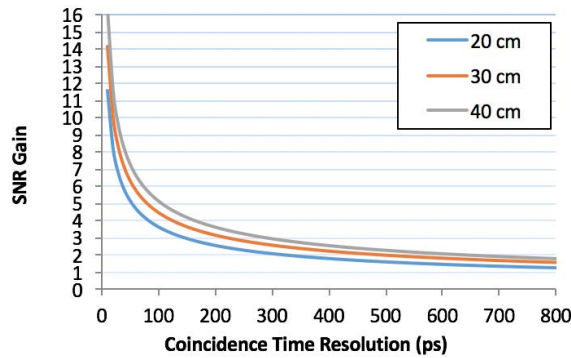
Fig. 1. SNR improvement as compared to non TOFPET as a function of the CTR for three different diameters of the FOV.
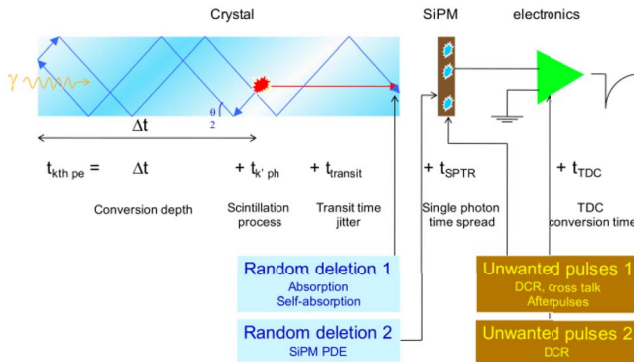

Fig. 2. Scintillator detection chain showing the different contributions to the time jitter at the level of the γ conversion, scintillation mechanism, light transport in the crystal, light photoconversion, and readout electronics.

The possibility to see in real time the accumulation of the events during the acquisition could introduce a paradigm shift in routine clinical protocols, allowing in particular to adapt the acquisition time to what is really observed and not to some predetermined evaluation. Moreover, such a timing resolution would allow recording the full sequence of all γ-ray interactions inside the scanner, including Compton interactions, like in a 3-D movie, opening the way to the integration of at least a fraction of the Compton events in the image reconstruction and to a further improvement in sensitivity.

The aim of this paper is to show that there are no physical barriers to reach this very challenging objective. Moreover, a number of enabling technologies are presently under development in the domain of metamaterials for the light production, photonic crystals for the light transport and multidigital photodetectors for the light conversion, which justify the launch of an official challenge for a 10 ps reconstruction-less TOFPET [7].

II. THE DETECTION CHAIN

In order to identify the parameters of interest to improve the CTR of a PET, is it essential to have a full and detailed description of the detection chain. A schematic of the sequence of processes associated to the detection of a γ-ray is shown in Fig. 2.

Several factors contribute to the time resolution of a scintillator-based γ-ray detection channel.

1) The fluctuation of the interaction depth of the γ-ray in the crystal. The 511 keV γ-ray entering in the crystal on the left of Fig. 2 will travel a certain distance in the crystal before interacting with it (red star on the figure), with an associated propagation time Δt. The probability of interaction is highest at the entrance of the crystal and decays exponentially at a rate depending on the absorption cross section in this material at the energy of the γ-ray. This fluctuation in the depth of interaction is not compensated by the corresponding fluctuation of the distance from this point of interaction to the photodetector, as the γ-ray travels at the speed of light, whereas the optical photons produced by the scintillator travel at the speed of light divided by the index of refraction of the scintillator, which is generally high (1.82 for LSO).

2) The scintillation mechanism, which is characterized by the emission of a sequence of optical photons, each one identified by its emission rank t, with a rise time τ_r and a decay time τ_d. The total amount of photons emitted defines the light yield (LY), each photon being characterized by its production rank k'.

3) The light transport from the emission point to the photodetector. This is an important contribution to the time jitter. Whether the detector head is fully pixellated (1-to-1 coupling to photodetector pixels) or using the block detector strategy (light sharing from a scintillator block to several photodetector pixels) the light transport is far from mono-mode and the emission of the photons being isotropic there are large variation between the different path lengths for the different photon trajectories. Two extreme cases are represented in red and in blue on Fig. 2. This results in a photon transit time spread (PTS), which plays an important role in the timing resolution. Moreover, the refractive index mismatch between the crystal and the coupling medium to the photodetector (typically close to 1.5) leads to a high probability for about 2/3 of the photons to bounce in the crystal up to several times before having a chance of being extracted. In addition to increasing the PTS, a longer path length increases the probability for the photons to be absorbed through a random deletion process (i.e., not correlated to the photon emission rank), affecting therefore the light transfer efficiency (LTE) to the photodetector and the timing resolution through the impact of these losses on the photo-statistics.

4) Once extracted from the crystal another random deletion process limits the number of the photons, which will be converted into photoelectrons in the photodetector. Although much progress has been made in photomultiplier technology, we have chosen here SiPMs because of their compactness, immunity to magnetic field, cost effectiveness, and their promising progressing curve for timing performance. The photo-detection efficiency (PDE) is another important parameter to be optimized in the quest for fast timing and is the product

of the geometric fill-factor of the sensitive parts of the SiPMs [individual avalanche cells: single photon avalanche detectors (SPAD)] by the quantum efficiency of the SPADs, which is related to the probability for a given photon to generate an avalanche in this SPAD. Impressive progress has been made on the PDE, which has been increased from about 20% to 55% in a few years-time only [8]. But nearly half of the photons will be lost in the conversion process and not produce any photoelectron signal, which are the actual carrier of timing information. For those, which will be converted, an avalanche will be produced in the SPADs and generate an electric pulse with a characteristic pulse shape. As the avalanche is a stochastic process there are fluctuations between different avalanches generated in the same conditions. This is reflected by another important parameter, which quantifies the single photon time response (SPTR) of the SiPM. It must be added that, in addition to the avalanches triggered by the photons from the scintillator, the SiPM generates also two sources of noise, which mimic the photon-triggered avalanches. The first one is the dark count rate (DCR), which can be considered as uncorrelated noise. On the other hand, the second one is related to cross talk and after pulses, generated by red and infrared photons produced by the avalanche, which can trigger secondary avalanches. This second source of noise is of course correlated to the signal.

5) Finally, a front end electronics with single or multiple time-digital-converters (TDC) connected to the SiPM will determine the arrival time of each photon or of the time when the integrated pulse reaches a predetermined detection threshold. The resolution of the TDC is another contribution to the timing uncertainty and the noise introduced by the front end electronics another source of unwanted pulses.

In summary the time estimator has to be extracted from a series of timestamps $(t_{k_{th}, pe})$, associated to each photoelectron produced by the acquisition chain. They are somehow related to the production of the scintillation photons but in a sequence modified by the light transport, different sources of losses and a random addition of noise generated pulses.

The photon counting statistics sets the ultimate limit to the timing performance, which originates in the statistical fluctuations of the timestamps associated to the registration of individual photons, as explained in [9]–[11]. From an ordered set of timestamps

$$T_{(N)} = \{t_{(1)}, t_{(2)}, \ldots, t_{(n)}\} \tag{2}$$

the goal is to extract the probability density function

$$f_{(n)|N}(t|\Theta) \tag{3}$$

describing the distribution of the nth order statistic, i.e., the probability for the n_{th} detected photon out of a total number of N photons emitted by a γ interaction at time Θ to be detected at time t. This provides the so called Fisher information $I_{T(N)}(\Theta)$. We can then define the Cramér–Rao lower bound, using maximum likelihood methods to minimize the
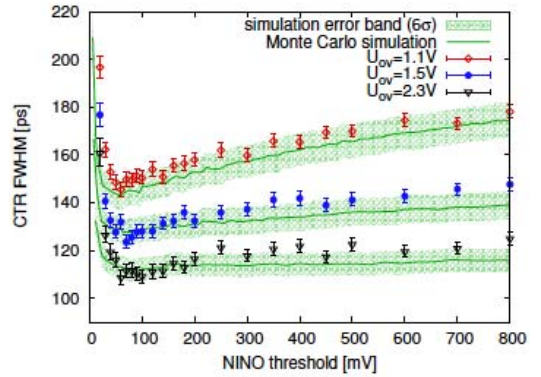

Fig. 3. Comparison of simulated CTR values with experimental ones as a function of the NINO discriminator threshold for three different bias overvoltages (from [12]).

variance of the time estimator Ξ, which sets the ultimate theoretical achievable timing resolution of the detection chain

$$\mathrm{Var}(\Xi) = 1/I_{T(N)}(\Theta). \tag{4}$$

III. SIMULATIONS

A. Simulation Tool

In order to optimize the key parameters influencing the timing resolution of a SiPM-based scintillation detector and to understand their relative importance and possible interplay it is necessary to develop a comprehensive model of all the components of the detection chain. Several attempts have been made in the past [9]–[11] but they were mostly considering the scintillator pulse shape and the photo-conversion process and lacking a full description of the photon transport in the detection system. More recently, a complete simulation tool based on Monte Carlo has been developed [12], which includes in a comprehensive model.

1) The fluctuation in the depth of the γ-ray interaction.
2) The scintillation statistics.
3) The photon propagation and losses in the crystal (similated by SLITRANI [13]).
4) The photodetector properties such as the PDE and the SPTR.
5) The signal pile-up considering the single cell pulse shape of the SiPM.
6) The DCR and optical cross-talk of the SiPM.
7) The bandwidth and noise of the readout electronics.

B. Predictions for LSO-Type Crystals

When introducing in the model precise measured values of some parameters, such as the scintillator LY, rise time and decay time, the SPTR, PDE, and single photon pulse shape of the SiPM, as well as the electronics noise, we can compare the predicted CTR of different detector chain configurations to the measured values. Fig. 3 shows the excellent prediction power of the simulation tool, when using a readout electronic chain based on the fast and low noise NINO discriminator developed at CERN for the Large Hadron Collider experiment Alice and fully described in [12].
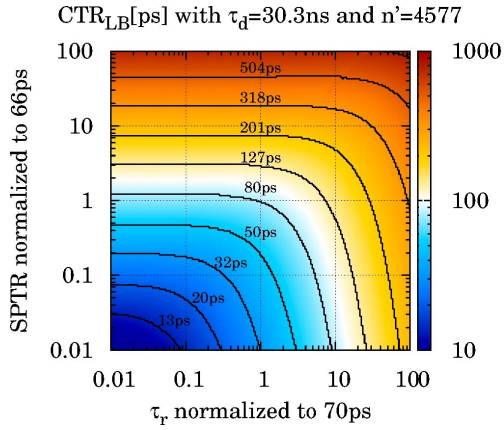
Fig. 4. Cramér–Rao lower bound calculations reveal the importance of the scintillation rise time if other factors like the PTS and SPTR start to be negligible (from [14]).

Fig. 5. Cramér–Rao lower bound calculations for a hypothetical 0 mm long LYSO:Ce scintillator with zero PTS and 100% LTE when 0, 1, 100, and 500 prompt photons are generated in addition to the LYSO scintillation pulse (from [14]).

It is then possible on this basis to quantitatively assess the impact on the timing resolution of a possible improvement of some parameters of the different components of the detection chain. In first approximation and when considering the crystal only, the CTR is proportional to the time density of the photons in the leading edge of the scintillation pulse [14]

$$CTR \propto \sqrt{\tau_r \cdot \tau_d / N_{phe}} \qquad (5)$$

where τ_r and τ_d represent the scintillator rise and decay time, respectively, and, N_{phe} the number of photoelectrons detected by the photodetector. The best scintillators used in modern PET scanners are close to the LY theoretical limit and the PDE of the last generation of SiPM is as high as 55%, which means that only small improvements can be expected on N_{phe} [8]. The effort should be focused therefore on the timing characteristics of the scintillator light pulse.

Fig. 4 gives an example of the evolution of the CTR Cramér–Rao lower bound when the scintillator rise time and SiPM SPTR are varying by two orders of magnitude around the measured values (normalized to 1) of 70 ps for the LSO rise time and 66 ps for the SPTR of the Hamamatsu SiPM.

For these two normalized values the CTR Cramér–Rao lower bound is 80 ps as can be seen on Fig. 4. We observe, however, that without changing the SPTR of the SiPM (1 in the figure), an improvement in the scintillation rise time (τ_r) would only improve the CTR by less than 10 ps (about 10%) and saturate at this level, which is in agreement with our measurements. However, if the SPTR could be reduced by two orders of magnitude and have therefore a negligible impact on the timing resolution, a reduction of the scintillator rise time by one order of magnitude would improve the CTR from 32 to 13 ps, i.e., a factor of nearly 250%. In this case the CTR would be proportional to the square root of the scintillation rise time, that is

$$CTR \propto \sqrt{\tau_r}. \qquad (6)$$

This clearly shows that both the scintillator rise time and the SPTR of the SiPM play a parallel role in the timing resolution, as both intro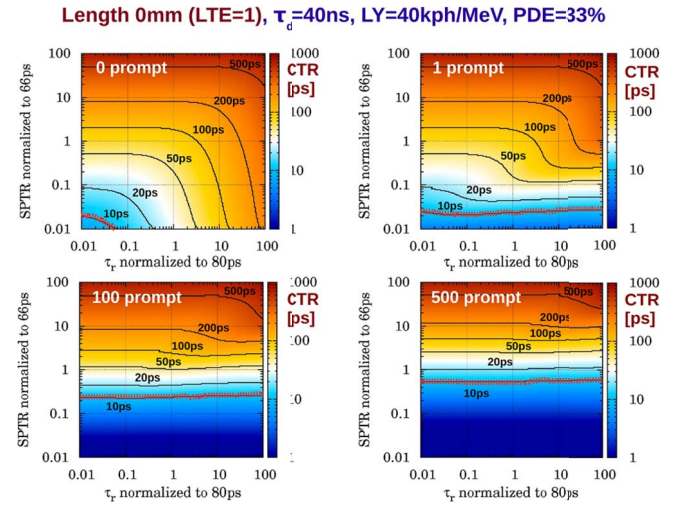duce a delay in the arrival of the first detected photoelectrons, which are the most significant carriers of the timing information.

As it will be shown in the next section, steady progress in the understanding of the scintillation mechanism in some crystals and the possibility of engineering the scintillators by using co-doping procedures have led to a significant reduction of the scintillation rise time. For instance we have measured a rise time of 36 ps in LGSO:Ce because of the positive action of gadolinium for transferring the excitation charge carriers to the Ce^{3+} activator ion and as low as 21 ps in LSO co-doped with Ce and 0.4 atomic % of Ca [14].

C. Role of Prompt Photons

This very precise Monte Carlo was also a precious tool to study the influence of prompt photons, generated in addition to the scintillation pulse, on the timing resolution. We know that such photons exist, produced by the Cerenkov emission from the photoelectric recoil electron in the dense and generally high refraction index scintillator material. Other mechanisms for generating more prompt photons are being studied (see the next section).

In the ideal case, where the light transport in the crystal can be considered without light loss and without introducing a PTS (LTE = 100%, PTS = 0) the expected CTR is depicted in Fig. 5 for LYSO, the most commonly used crystal in PET scanners with an LY of 40 000 ph/MeV, a decay time of 40 ns and a rise time normalized to a measured value of 80 ps. A conservative value of 33% has been chosen for the SiPM PDE and the SPTR has been normalized to the measured value of 66 ps. Fig. 5 shows the expected CTR in 4 different cases corresponding to the addition production of 0, 1, 100 and 500 prompt photons (in addition to the LYSO scintillation light), respectively.

It is seen that in this ideal case the production of one prompt photon is sufficient to improve the CTR at the nominal value of the rise time, provided the SPTR of the SiPM can be
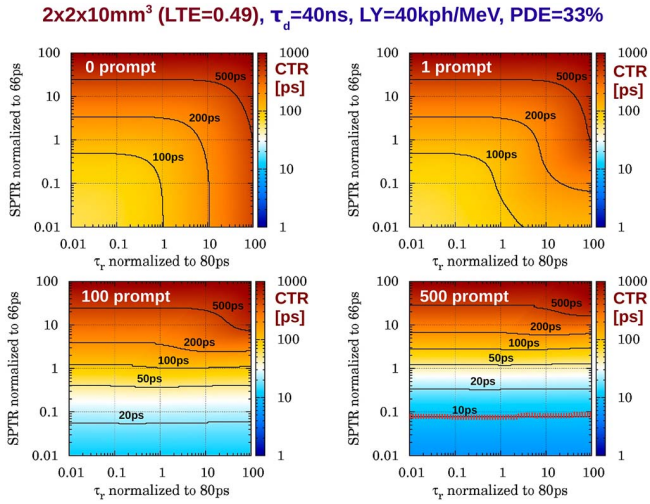
2x2x10mm³ (LTE=0.49), τ_d=40ns, LY=40kph/MeV, PDE=33%

Fig. 6. Cramér–Rao lower bound calculations for an LSO:Ce scintillator with $2 \times 2 \times 10$ mm³ size. In this case at least 500 prompt photons and a low SPTR (sigma) are needed to achieve a CTR of 10 ps FWHM. This is caused by the photon travel spread and light absorption (LTE = 0.49) in the crystal (from [14]).

Fig. 7. Cramér–Rao lower bound calculations for $2 \times 2 \times 3$ mm³ and $2 \times 2 \times 2 \times 20$ mm³ LSO:Ce,Ca scintillator with a SiPM having a PDE of 55%, as a function of the number of additional prompt photons generated (from [14]).

reduced by at least one order of magnitude. The production of 500 prompt photons would allow to reach 20 ps CTR full width at half maximum (FWHM) at the nominal values of the scintillator rise time and SiPM SPTR, and 10 ps if the SPTR can be reduced by a factor of 2.

The situation deteriorates of course for the case of a $2 \times 2 \times 10$ mm³ crystal if we introduce in the Monte Carlo the measured value of the LTE of 49% and if we take into account the PTS from the light ray tracing program in a crystal of these dimensions wrapped with Teflon. The results in Fig. 6 show that even with 500 prompt photons generated, the best achievable CTR at the nominal scintillator rise time and SiPM SPTR, is about 40 ps FWHM. Reaching 10 ps would require a reduction of the SPTR value by at least a factor of 10.

If we now introduce the parameters of the co-doped LSO:Ce,Ca, which in spite of a slightly lower LY of 32 000 ph/MeV has a much improved rise time of 21 ps and a slightly shorter decay time with two components at 33 ns (84%) and 8 ns (6%), readout by the last SiPM generation [8], exhibiting a PDE of 55% at the wavelength emission of LSO (420 nm), we have the situation depicted on Fig. 7. This figure shows the expected CTR for two crystals of 3 and 20 mm length, respectively, as a function of the number of prompt photons generated in addition to the LSO scintillation light. The horizontal axis is centered at 20 photons, as this is the average number of Cerenkov prompt photons generated by the recoil electron of a γ-ray interaction in such a crystal.

The influence of the crystal length through the introduction of the PTS in the photon transport and of an LTE reduced to 39% only in a 20 mm LSO co-doped crystal clearly appears when comparing the two plots and needs to be compensated by the production of a larger amount of prompt photons to reach the same timing performance. However, the better timing performance of LSO:Ce,Ca crystals allows reaching the 10 ps target with 20 mm long crystals with about the same number of additional prompt photons than for 10 mm long standard LSO or LYSO crystals.
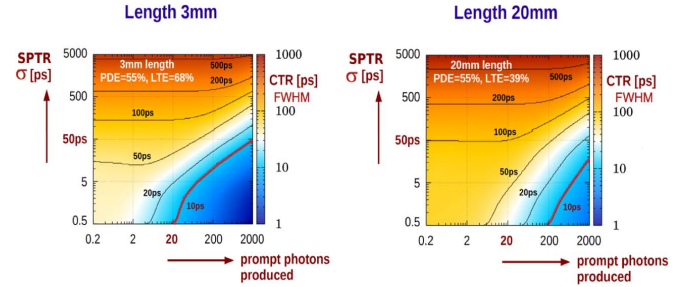
If on the other hand specific treatments applied to the crystals could be developed to reduce the PTS and the light output reduction in long crystals the impact of the crystal length on the timing resolution could be reduced, which would relax the requirement on the number of prompt photons to a few hundreds.

Some ways to produce prompt photons in a scintillator, to reduce the impact of the crystal length on the timing resolution and to decrease the SPTR of SiPMs will be introduced in the next section.

IV. SCINTILLATION RISE TIME AND DIFFERENT SOURCES OF PROMPT PHOTONS

A. Scintillator Rise Time and Cerenkov Photons

The scintillation light produced by an inorganic scintillator results from a complex sequence of relaxation mechanisms of the hot electron-hole pairs produced by the interaction of ionizing radiation with the scintillator crystal before the luminescent centers of the scintillator can be activated. This relaxation process has been described in detail in [15] and [16] and is at the origin of the scintillation rise time (τ_r), which delays the emission of the first produced photons, increases their time jitter and reduces accordingly the time resolution of the scintillator.

The process being stochastics large statistical fluctuations are therefore induced for the generation of the first scintillation photons, which set an intrinsic limit to the time resolution that can be achieved by a scintillator. In order to evaluate this limit, the rise time of several scintillators has been measured with a precision time correlated single photon counting bench described in [14]. The results, shown in Fig. 8 for the lutetium orthosilicate family, show that the average value of the measured rise time for LSO:Ce and LYSO:Ce from different producers is around 70 ps. This value can be significantly decreased if a co-doping strategy is adopted, resulting in a rise time of 36 ps in the for LGSO:Ce and 21 ps for LSO:Ce,Ca, gadolinium and calcium playing the role of a bridge easing the charge transfer process to the Ce^{3+} activator ion.

Interestingly, when measuring crystals having a slower rise time, such as LuAG:Pr, a sharp peak is visible in the early part of the light pulse shape, clearly separated from the scintillation rising part of the pulse (Fig. 9). A detailed analysis showed that this peak can be attributed to a small number (3.4 on average)
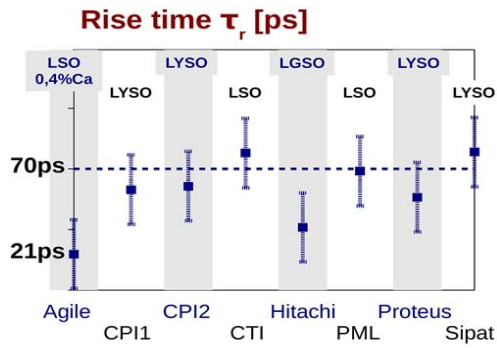
Fig. 8.   Measured scintillation rise times for the different lutetium orthosilicate crystals from different producers (from [14]).

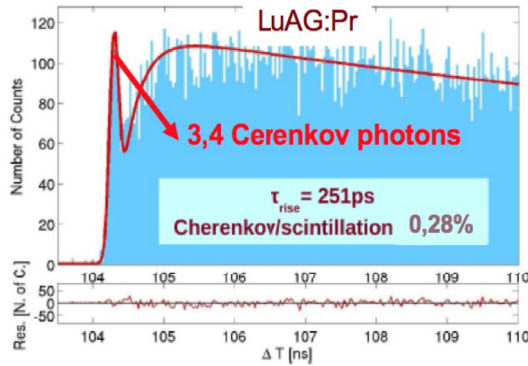Fig. 10.   Normalized IBL spectra of $CaWO_4$, $BaWO_4$, and $SrWO_4$ (from [19]).

Fig. 9.   Measured and fitted photon emission rate in LuAG:Pr with a prompt photon peak (left) compatible with the recording of an average of 3.4 Cerenkov photons per γ-ray interaction event (adapted from [14]).

of Cerenkov photons emitted by the recoil electron produced by the γ-ray photo-electric interaction [17].

Moreover, it was shown in [17] that these Cerenkov photons contribute to a small improvement from 340 to 290 ps (w/0 and with Cerenkov photons, respectively) of the CTR of two such crystals. The number of Cerenkov photons produced by a 511 keV γ-ray in the majority of scintillators used in PET scanners is of the order of 20. However, as most of them are produced in the UV part of the spectrum, where their detection efficiency is low, only a maximum of 5 are detected in practice. This number is obviously too small to have a strong impact on the timing resolution but this justifies the quest for other mechanisms of prompt photon production.

B. Hot Intraband Luminescence

When ionizing radiation interacts with an inorganic scintillator it produces hot electron-hole (eh) pairs, i.e., a hole in the deep core levels of the heavy atoms of the structure and an energetic electron in the upper level of the conduction band.

The standard scintillation mechanism involves a rather long (typically a few nanoseconds) relaxation process of this hot eh pair, with multiplication of the charge carriers by multiple scattering in a first phase, followed by phonon exchange with the crystal lattice in a second phase, before all the holes accumulate at the 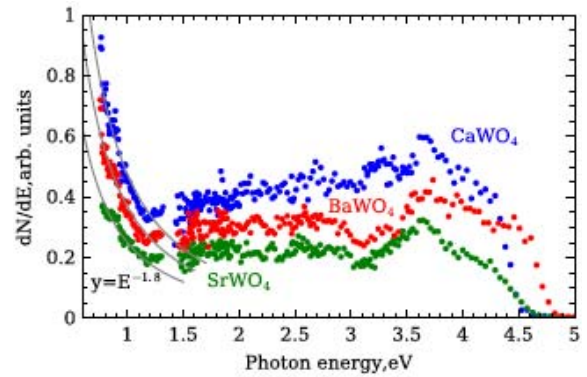top of the valence band and the electrons at the bottom of the conduction band. Only then, they can couple together and form excitons, which are at the origin of the scintillation. The large timing fluctuations in this ns relaxation process are at the origin of the observed rise time.

However, in some cases a prompt emission is possible, caused by radiative transitions of hot electrons [e-intraband luminescence (IBL)] or hot holes (h-IBL) between sublevels of the conduction or valence band of a crystal, respectively. This so called hot IBL takes place during the second phonon-assisted phase of the thermalization of these electric carriers, between 10^{-14} and 10^{-12} s, when their kinetic energy has dropped below the forbidden gap energy E_g after the multiple scattering phase.

The theory of this hot luminescence has been developed more than 40 years ago and experimental studies have been conducted with electron beams on alkali-halides crystals [18]. More recently a number of other crystals have been investigated, including RbCl, Al_2O_3, LYSO, CeF_3, PbF_2, BGO, and a number of tungstates: $PbWO_4$, $SrWO_4$, $CaWO_4$, $BaWO_4$ [19]. They all show similar features: a prompt and temperature independent emission in the ps range with a flat spectrum in the visible, limited on the UV side by the absorption edge of the crystal, and a steep onset in the near infra-red (NIR) below 1.5 eV (Fig. 10).

The LY and decay time are to a large extent determined by the competition between nonradiative phonon-electron scattering and radiative transitions between substates of the conduction and valence bands. As these radiative transitions can involve any of these substates distributed in an energy range of several eV, provided that the transitions are optically allowed, the IBL is characterized by a continuous spectrum extending from the far IR up to the transparency edge defined by the bandgap of the crystal.

The main process which controls the thermalization of the excitation is the rate of electron-phonon scattering in ionic crystals. Under the parabolic energy dispersion approximation, the rate of longitudinal optical (LO) phonon emission depends on the LO phonon energy $\hbar_{LO}$, the carrier effective mass and the effective dielectric permittivity describing the response of ionic subsystem of the crystal to electric field of the carrier. This rate is about 3×10^{14} s^{-1} for high $\hbar_{LO} = 100$ meV (fluoride and oxide crystals) and slightly lower

for low $\hbar_{LO} = 10$ meV (CsI). For a given kinetic energy of the electrons the relaxation time will be longer if the energy of the LO phonons is small, as a larger number of phonons (and therefore more interactions) will have to be produced to thermalize the electron. From the above numbers this time would be between 0.03 and 0.3 ps per eV of energy relaxation for fluoride/oxide crystals or CsI, respectively. For a 10 eV energy gap, as is the case for the majority of scintillating crystals, an emission in the ps range can be expected, as effectively observed [16]. It must be noted that the phonon scattering depends also on the mobility, and therefore, on the effective mass of the charge carrier. In most crystals the effective mass of holes is larger than that of electrons. Therefore, the relaxation of holes in the valence band is typically slower than the relaxation of electrons. This could provide an explanation for the NIR increase of the IBL, which could be attributed to the radiative transitions of hot holes in the valence band. Alternative explanations involve second-order perturbation theory with the simultaneous emission of a photon and a phonon associated to a hyperbolic emission spectrum as a function of the photon energy [19].

Comparing the average rate of nonradiative LO phonon emission to the rate of radiative dipole transitions of typically $10^8 - 10^9$ s^{-1} one can estimate the yield of IBL in the range of 10^{-3} to 10^{-4} of the total number of eh pairs produced in the crystal, i.e., a few tens of photons per MeV. At 511 keV this number is comparable to the Cerenkov emission discussed above, and therefore insufficient to expect a large impact on the timing resolution.

However, the precedent analysis has been made assuming a uniform density of states (DOS) in the conduction and valence bands for the e-IBL and h-IBL, respectively. This situation could change significantly for a nonuniform DOS, and even more in the case of a splitting of these bands. An interesting case, presently under investigation, is the one of ternary compounds, where the cation is linked to two different anions. The valence band is generally populated by orbitals of the anions. It is therefore interesting to look at some crystallographic configurations of ternary compounds, for which the orbitals of the two anions occupy different energy levels of the valence band. A systematic search has been made using the orbital calculation program: The Materials Project, freely available on the Web: https://www.materialsproject.org. A good example is given in Fig. 11 for two different configurations of barium oxy-halides.

In the case of Ba_4OCl_6 a splitting of 1 eV is observed between the oxygen and chlorine orbitals, whereas this splitting increases up to 2.5 eV when chlorine is replaced by fluorine in Ba_4OF_6. In this case the gap is large enough to considerably decrease the rate of hole-phonon scattering. If, in addition, the bands are flat enough to allow a delocalization of the electric carriers, every hole created in the bottom part will find a large amount of electrons available in the upper part to allow a fast radiative transition, providing this transition is optically allowed by the quantum selection rules.

This is a similar situation as for the cross-luminescence, where a fast scintillation can be observed in some crystals as a result of the recombination of a hole from the upper core
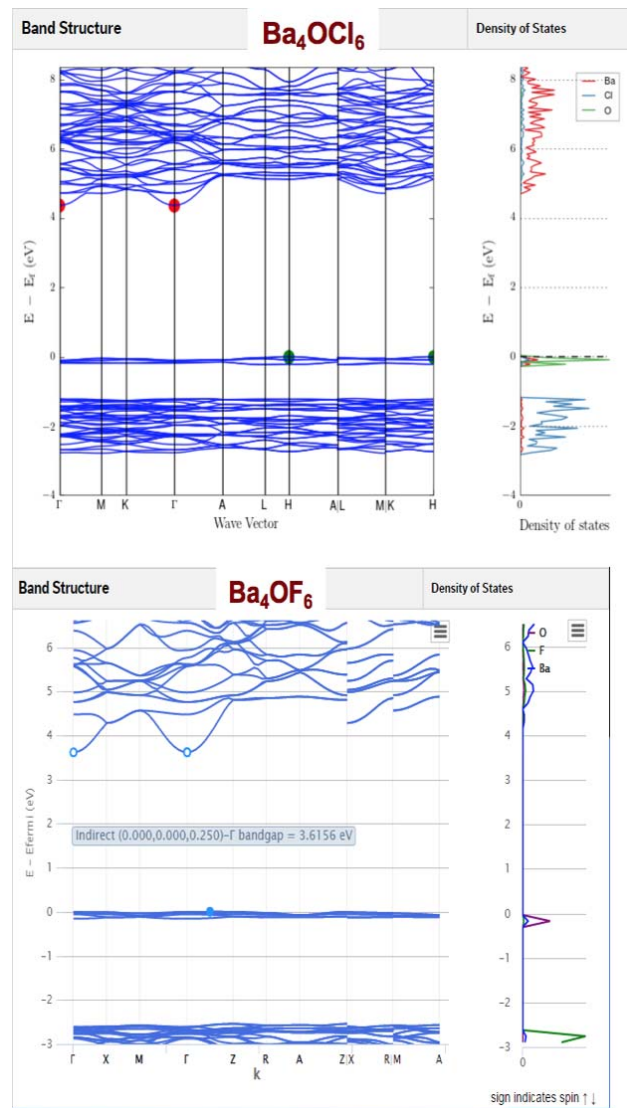

Fig. 11. Band structure of Ba_4OCl_6 and Ba_4OF_6 showing a splitting of the valence band of 1 eV and 2.5 eV, respectively.

level in the crystal with an electron from the valence band, providing the energy gap between these two levels is smaller than the band gap between the valence and the conduction band to suppress the competing non radiative Auger emission. This is the case for BaF_2, which exhibits a 600 ps cross-luminescent emission, but in the deep UV, where the detection efficiency is low, in contrast to IBL, where the emission is in the visible to NIR spectrum.

In the same category of fast intra-band luminescence another interesting mechanism of fast emission may well come from direct band-gap transitions in semi-conductors. In the presence (natural or created by specific doping) of a donor band in the vicinity of the conduction band in semiconductors such as ZnO or CdS a very fast subnanosecond band-to-band recombination process is observed. First discovered in the 1960s by Lehmann [20], this process was reintroduced by Derenzo *et al.* [21] a few years ago and seems to apply also to heavier materials like CuI, PbI_2, and HgI_2.

In such materials fast near band-edge transitions are observed as a result of a high density of e-h pairs generated by ionizing radiation because of the low band gap and of the donor band providing a large number of electrons opening the possibility of nongenuine e-h pair recombination. This emission arises from band-to-band or free exciton recombination transitions. If the transition is direct and parity allowed, the radiative lifetime can be very short, one nanosecond or less.

Owing to the low band-gap in semi-conductors the emission is generally in the red near-infrared region (2 eV to 2.5 eV). An important limitation is a severe temperature quenching in several scintillators due to the presence of impurities and a number of traps close to the energy levels active for the fast radiative transitions.

C. Quantum Confinement in Nano-Scintillators

Another way to produce prompt photons is to develop hetero-structures based on a combination of standard scintillators (such as LSO or LYSO) and nanocrystals. Nanocrystals have gained considerable attention over the last two decades because of their excellent fluorescence properties. In such systems quantum confinement offers very attractive properties, among which a very high quantum efficiency and ultrafast decay time. Moreover, they have a broadband absorption and narrow emission, enhanced stability compared to organic dyes, and the fluorescence is essentially tunable from the UV, over the visible, to the near-infrared spectral range (300 nm–3000 nm) by nanocrystal size and material composition.

High quality semiconductors, e.g., GaAs or CdSe, based on nano-structures have an LY that can reach 70%–80% of absorbed energy as compared to at most 15% in standard scintillators such as LSO or $LaBr_3$. Moreover, the emission lifetime is usually shorter than 1ns. These impressive performances are attributed to electron confinement, phonon confinement and optical resonances taking place in these nano-materials. Embedded in meta-structures based on polymers or heavy scintillators (such as LSO, LYSO or heavy scintillating glasses) they could complement the standard scintillation signal with a very fast light component that could be exploited for reaching an ultimate timing resolution.

Bright and transparent ZnO:Ga polystyrene composites prepared by homogeneous embedding ZnO:Ga nano-crystals into a scintillating organic matrix [22] have shown an ultrafast sub-nanosecond luminescence as measured by the author and his group and shown in Fig. 12.

A novel route toward the realization of ultrafast timing resolution is possible with the use of colloidal CdSe nano-sheets (CQwells) [23], a new class of 2-D materials. CQwells are solution-processed analogs to epitaxial quantum wells (Qwells), but because they are synthesized in solution, they can be deposited on any substrate with any geometrical configuration. Further, a large dielectric mismatch between the inorganic CdSe CQwells and the surrounding organic environment results in much stronger quantum confinement than in epitaxial Qwells. This mismatch combined with very little dielectric screening due to the 1.5 nm CQwell
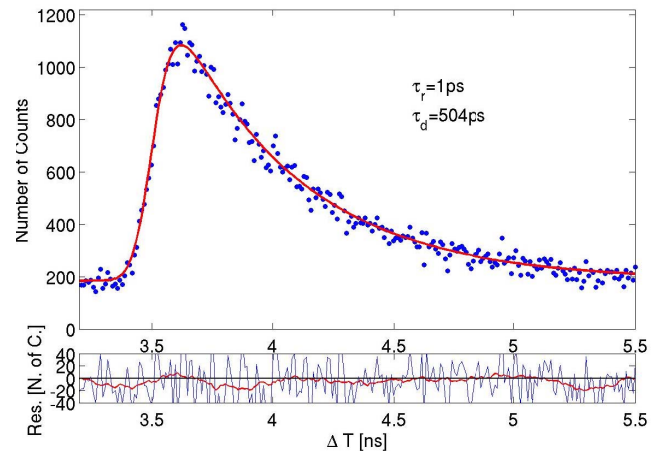

Fig. 12. Pulse shape of 1 mm thick polystyrene slab with 10 wt% of ZnO:Ga nanocrystals under picosecond X-ray excitation (adapted from [14]).
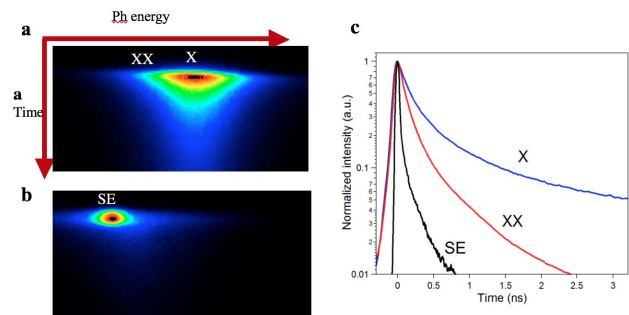

Fig. 13. Time-resolved spectral decay under femtosecond excitation. (a) Streak image showing the spectral decay of exciton (X) and bi-exciton (XX) emission from CdSe CQwells. (b) Stimulated emission at an ultralow excitation fluence of $F_0 = 6$ μJ/cm^2, with characteristic spectral narrowing and lifetime shortening. (c) Decay time curves of the exciton X, the bi-exciton XX and the stimulated emission SE.

thickness results in strongly enhanced exciton and bi-exciton (bound state of two excitons) binding energies of 132 and 30 meV, respectively, making both populations stable at room temperature.

The strong electron and hole confinement in one dimension and free motion in the plane has several important consequences, including strict momentum conservations rules (in contrast to quantum dots) and a giant oscillator strength transition. Momentum conservation in CQwells limits the available states for Auger transitions, reducing the recombination rate of this nonradiative channel. In addition to the enhanced exciton and bi-exciton binding energies, a giant oscillator transition results in radiative lifetimes that are significantly shorter than in bulk CdSe (∼400 and ∼100 ps, respectively). All of these properties contribute to the ultralow threshold for stimulated emission (or super-luminescence) with sub-ps decay time that has been observed with these CQwells and described in [24]. Streak camera images obtained in the author's lab are shown in Fig. 13. Such systems could find interesting applications in ultrafast X-ray imaging as well as for providing a fast time tag in γ imaging if used in hetero-structures in combination with dense scintillators like LSO with a structuration dimension of
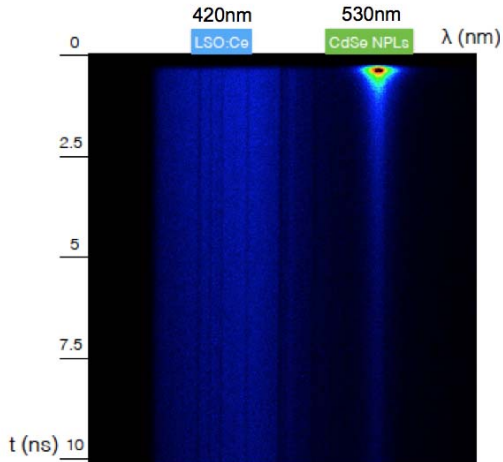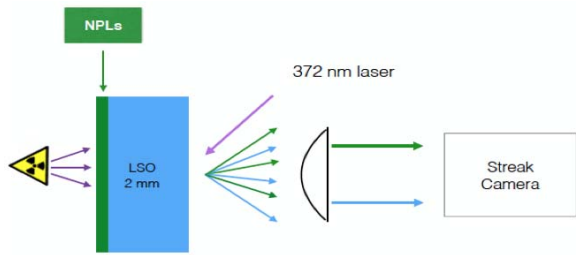
Fig. 14. Example of an hetero-structure made of a 2 mm thick slab of LSO crystal with a 100 μm layer of CdSe nano-sheets excited by a pulsed X-ray source. The streak camera image at the bottom shows on a vertical 10 ns scale the long LSO scintillation centered at 420 nm and the much shorter sub-ns emission from the CdSe CQwells at 530 nm. The long tail at 530 nm corresponds to the CQwell emission under excitation by the LSO scintillation light. The black vertical lines are artifacts caused by dust on the entrance slit of the spectrophotometer (from [24]).

the order of the recoil electron range, as suggested in [25] and shown in [24, Fig. 14].

V. LIGHT TRANSPORT AND PHOTONIC CRYSTALS

A. Light Transport in the Crystals

As already explained in Section II, another key issue affecting time resolution of a scintillator is the inefficiency of light extraction from materials with a high index of refraction. This not only leads to a reduction of light collected at the photo detector, with consequences on the photo-statistics, but also to an increase of the path length of the photons due to multiple light reflections within the scintillator in the case of scintillator pixels, which further increases the probability of absorption but also increases the PTS, which can contribute to as much as 150 ps FWHM in a $2 \times 2 \times 20$ mm^3 LSO pixel. The influence of the crystal length has been studied in detail in [26].

Fig. 15 shows on the left panel the deterioration of the CTR as a function of the crystal length for LYSO:Ce and LSO:Ce,04%Ca crystals. The difference in CTR between the two crystals seems to decrease for longer crystals, which can be explained by the higher self-absorption of LSO:Ce, 04%Ca, as shown on the right panel. As shown in Fig. 7 the LTE for this crystal decreases from 68% to 39% when going from
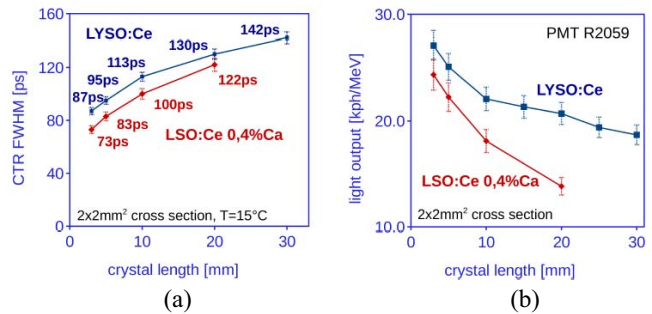

Fig. 15. (a) CTR versus crystal length for LYSO:Ce and LSO:Ce,0.4%Ca. (b) Measured light output versus the crystal length for LSO:Ce:0.4%Ca and LYSO:Ce revealing a higher light absorption for LSO:Ce,0.4%Ca (from [8]).

3 mm to 20 mm long crystals. When correcting the CTR curves from the photo-statistics impact of the decrease of the light output, about half of the CTR deterioration as a function of the crystal length can be explained. The second half corresponds to an increase of the PTS for longer crystals.

The large discontinuity in the refractive index at the scintillator-photodetector interface is the primary cause of the inefficient detection of the scintillation light. The light collection efficiency depends on: 1) the angular distribution of scintillation photons incident on scintillator-photodetector coupling interface; 2) the transmission at the angle of photon incidence; and 3) the probability of a photon reflected back into the bulk crystal to reappear at the interface.

B. Photonic Crystals

A possible solution has been proposed to overcome the problem of total internal reflection in scintillators and to improve the light extraction efficiency at the crystal/photo detector interface by means of photonic crystals (PhCs), i.e., media with a periodic modulation of the dielectric constant [27]. By means of photonic nano-structuring of the different surfaces of the scintillator, the light transport can be optimized, which has a direct impact on the timing and LY performance of the detector.

Photonic crystals are natural or artificial materials which have a periodic arrangement of different dielectric materials in one, two, or three dimensions. The spatial arrangement hereby is in the range of the wavelength of the photons. While PhCs can be found in nature in various forms (e.g., opals or butterfly wings) PhCs were described for the first time in 1987 by Yablonovitch [28] and John [29]. Their intention was to develop a material showing similar effects on photons as semiconductors on electrons. Many applications were arising from this basic idea but the principle of PhCs is always the same: light is scattered at the interfaces where the index of refraction changes and the scattered waves can interfere constructively or destructively with each other. The stationary properties of the light that are allowed to travel are called modes. While the modes of propagation in a homogeneous medium are plane waves, the modes of a periodic medium are known as Bloch modes. A Bloch mode can be seen as a standing wave field produced by the multiple coherent scatterings of a wave by the periodic structures of a PhC lattice.
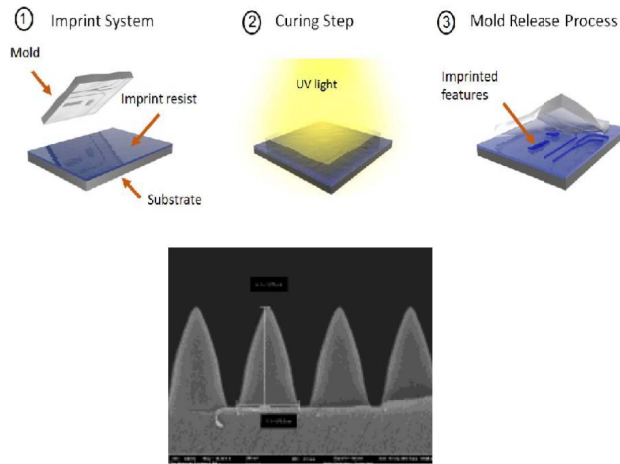
Fig. 16. Schematic of the nanoimprinting process used for fabricating the PhCs. Scanning electron microscope image of the pattern on the right panel. The nano-cones have a period of 880 nm, and a height of 1275 nm (from [30]).

Fig. 17. ^{137}Cs spectra of nonimprinted (red curve) and nanoimprinted (blue curve) GYGAG. Imprinting was carried out in CP5 polymer having refractive index $n = 1.875$ @ 550 nm (from [30]).

Fig. 18. PDE of FBK NUV-HD at different over-voltages. Courtesy of C. Piemonte (FBK).

Several approaches have been investigated to develop a scalable and cost effective way to produce photonic crystals, including nanoimprint technologies, interference lithography, and colloidal lithography. The photonic crystal pattern can be directly engraved on the scintillator but it is more flexible to deposit first a substrate layer on the crystal of the right thickness (typically a few hundreds of nm) and refractive index as the performance of the PhC depends on the refractive index of the PhC substrate, which should ideally be higher than the one of the scintillating crystal. This substrate is then etched with standard lithography techniques after imprinting a resin deposited on its surface with a patterned silicon stamp. Alternatively, some substrates can be directly imprinted with a silicon stamp or a replica of it following a promising route developed in the frame of a collaboration between CERN and the companies radiation monitoring devices and Abeam technologies in USA. In this case, the PhC substrate is a high refraction index polymer, specifically developed by the company Abeam technologies [30]. Fig. 16 shows a schematic of the imprinting process.

Using nanoimprinted PhCs produced by this method, enhancements in the scintillation light extraction by over 40%, and in the energy resolution, ranging from 9%, as shown in Fig. 17 to nearly 40% for LSO (compared to the standard grease-coupling), have been experimentally demonstrated [30]. The impact on the timing resolution is presently under investigation but it is expected to be at least proportional to the square root of the light output gain, an effect related to the gain in photo-statistics. Preliminary measurements indicate that it is in fact likely to be higher, as the PhCs not only increase the number of extracted photons, but increases also the time density of the extracted photons by considerably reducing their average path length, as a result of a strong reduction of multiple bouncing within the crystal. More details on the photonic crystals are given in the review paper [31] and the references herein.
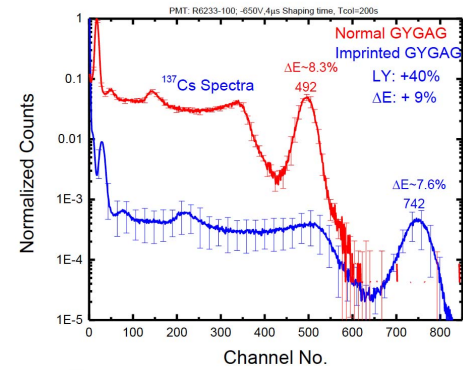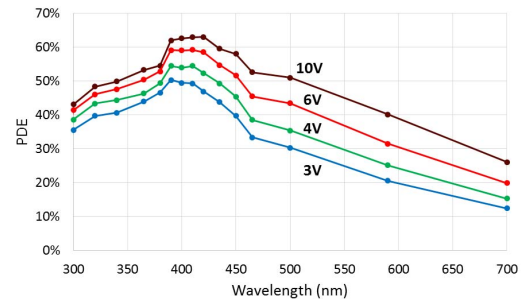
VI. SILICON PM AND ELECTRONICS

A. Progress on SiPM Performance

SiPMs experienced enormous technological advancement in the past years enabling highest CTR of 73 ± 2 ps FWHM for $2 \times 2 \times 3$ mm^3 and 117 ± 3 ps for $2 \times 2 \times 20$ mm^3 LSO:Ce, 0.4%Ca crystals readout by optimized electronics in the lab [17].

In particular the PDE is an important factor for the timing resolution of the scintillator-based detection chain as it directly influences the number of photoelectrons produced and therefore the photo-statistics. It is defined as the product of the fill factor of the sensitive parts of the SiPM, made of a number of individual SPADs working in Geiger mode, by the quantum efficiency of these SPADs. The PDE has been increased in a few years-time from about 20% up to 55 to 65% by the majority of the producers. Fig. 18 shows an example for the Fondazione Bruno Kessler (FBK) near ultra-violet (NUV)-HD SiPM at different over-voltages.

As it was shown in Section III and Fig. 4, the CTR improves as the square root of the scintillator rise time up to the point where the rise time becomes comparable to the SPTR of the SiPM. Scintillator rise time and SPTR play indeed a symmetric role in the time resolution and it can be shown that the CTR is also proportional to the square root of the SPTR. As a result of this, a parallel effort must be made on the scintillator rise time and on the SiPM SPTR. Most of the SiPMs produced today by different producers have an SPTR in the range of 60 to 80 ps sigma. Fig. 4 clearly shows that this sets the Cramér–Rao limit of the timing resolution at the level of about 80 ps, whatever
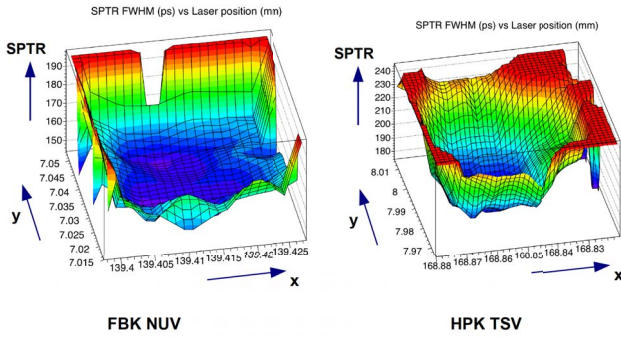
Fig. 19. Single photon scan across an SPAD of an FBK NUV and Hamamatsu last generation SiPM, showing a deterioration of the SPTR on the edge of the SPAD due to space charge effects.
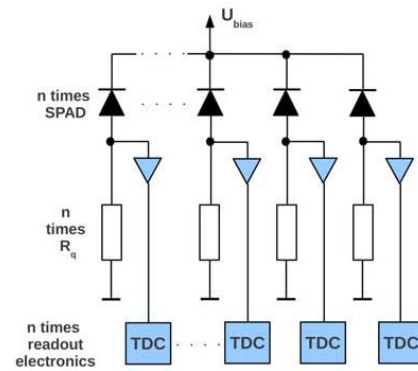

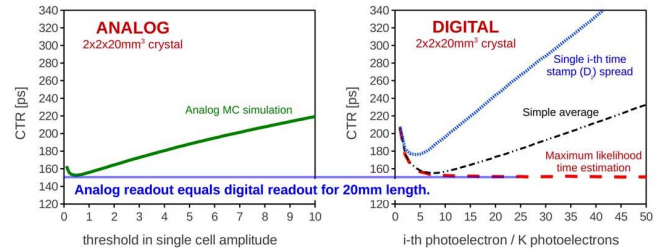Fig. 20. MD-SiPMs, where the timestamp of every photon detected is recorded with its own TDC.

Fig. 21. Analog and MD-SiPM simulations for a crystal with dimensions of $2 \times 2 \times 20$ mm^3. In the simulations we set to zero the DCR and the crosstalk of the SiPM as well as the electronic noise. The simulation error is in the range of 5%, not including parameter uncertainties (from [35]).

the progresses that could be made on the rise time of the scintillators.

Several factors contribute to the SPTR, the most critical ones are as follows.

1) The individual SPAD intrinsic resolution, related to the timing characteristic of the avalanche development, which depends on the SPAD design.
2) The baseline noise fluctuation of the SiPM, which depends on the area of the photo-sensitive part of the SiPM and the number of SPADs.
3) The total capacitance of the SiPM, which also depends on the area of the photo-sensitive part of the SiPM and the number of SPADs.

In order to evaluate the ultimate timing performance a SiPM could reach some tests have been made by the author and his group on different stand-alone SPADs produced by FBK (10 μm and 30 μm diameter) and illuminated with a single photon source provided by a picosecond laser with a known time jitter of 42 ps [32]. With such an experiment the contributions arising from signal transit time spread and the influence of capacitance, dark counts, after-pulse, and crosstalk due to multiple SPADs are discounted. After removing the laser and readout electronic jitter (42 and 21 ps, respectively) to the measured value of 52 ps FWHM, the intrinsic SPTR value could be extracted. Its value of 22.3 ps FWHM or 9.5 ps sigma defines the ultimate timing resolution for this kind of SPAD.

Moreover, scanning the laser spot across the SPADs of SiPMs from different producers revealed a nonuniformity of the response as a function of the impact point of the photon, showing that further improvements are still probably possible with a proper design of the SPADs (Fig. 19).

As a conclusion of this paper it clearly appears that the mechanisms of Geiger avalanche in silicon has the potential of 10 ps STPR, which is compatible with the TOFPET 10 ps challenge. However, the SiPM timing resolution is presently limited by system effects resulting from the parallel connection of a large number of SPADs in large area SiPMs with a consequent increase of the dark count noise, overall capacitance, as well as after-pulse and cross-talk probability.

B. Digital Versus Analog SiPM

In order to alleviate this problem some people are proposing another technique to detect the scintillation photons by means multidigital SiPMs (MD-SiPMs) [33], [34], as shown in Fig. 20. In these purely digital devices every photoelectron detected in an SPAD is registered with its own timestamp, thus providing the maximum information of the scintillation photon rate. Moreover, the timing information from each scintillation photon is extracted as close as possible from the individual SPAD, where it has been produced.

Besides the considerations related to the integration of the SPADs in a SiPM and to the best layout to extract the timing information, a detailed study has been made to evaluate the relative merits of an analog versus a purely digital approach [35]. The avalanche pulse shape and the limited bandwidth of the amplifiers do not allow to follow each individual photon. Therefore, the time for the integrated pulse to reach a given threshold, even as low as a single photoelectron, depends on a weighted average of the time of arrival of several photons. Their number depend on the rate, at which they are detected by the SiPM. It is therefore difficult to associate an exact number of detected photons to a given detection threshold and this can be considered as a limit of the analog approach.

Results of a detailed Monte Carlo study reported in [35] show that the analog and multidigital readout of SiPMs can lead to very similar Cramér–Rao limits of the time estimators for LSO type crystals for both types of readout. The left panel of Fig. 21 shows the Cramér–Rao limit as a function of the detection threshold expressed in the single SPAD signal amplitude, which does not necessarily correspond to the number of detected photoelectrons. The right panel of this figures shows the results of the same calculations as a function of the rank of
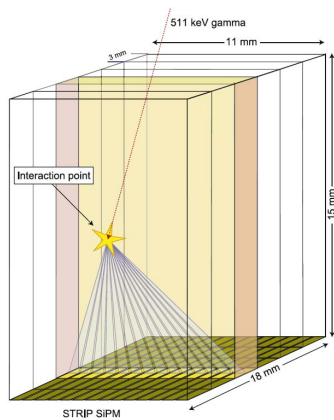
Fig. 22. Schematic representation of coupling of strip-SiPMs to an array of scintillating slabs (from [36]).

last detected photoelectron. In his case the simulation has been made considering only the time tag associated to this photoelectron but also to a simple average of the first photoelectrons time tags up to this rank, and finally using a maximum likelihood time estimate based on the all the photoelectron time tags up to the considered rank.

It can be seen that the digital readout of the SiPM with the maximum likelihood time estimator gives CTR values that are comparable to the minimum CTR of an analog SiPM with its SPAD signal pile-up and leading edge discrimination. However, the optimal CTR values in the analog SiPM, as well as for the simple average time estimation, are observed for a rather small range of threshold values (averaged timestamps), whereas the multidigital SiPM with the maximum likelihood time estimator provides a stable CTR estimate after about ten registered photoelectron timestamps. This is a significant advantage of the multidigital approach, which appears therefore more robust against electronic and detector noise.

One possible drawback of the multidigital approach is related to the higher amount of electronic circuits attached to each individual SPAD, which could compromise the PDE by the reduction of the fill factor in the case of a 2-D integration layout. However, the progress in through silicon via technology as well as in 3-D electronic integration could alleviate this limitation. Moreover, a 3-D integration strategy offers new possibilities to better thermalize and reduce the impact of a higher power consumption generally associated to a higher bandwidth. A number of groups and companies are presently working on different 3-D architectures, which could introduce a real breakthrough in SiPM technology.

As the cost is also an important issue some groups are also considering creative solutions to couple specially designed SiPMs to a matrix of crystals. An elegant solution is proposed in [36] where SiPM strips with differential readout (for a better control of the noise) at both ends, are coupled to a number of crystal slabs installed orthogonal to the strips (Fig. 22). Each strip runs as a transmission line, the difference of time between the two end of the strip identifying the crystal slab and the distribution of charge in the different strips allowing the reconstruction of the γ conversion point in the slab. From a precise knowledge of this interaction point the already

quite good timing resolution obtained (similar to the best analog SiPMs) can be further improved by applying corrections to take into account the travel time of the γ-ray inside the crystal as well as of the optical photons to reach the different strips.

VII. CONCLUSION

Results achieved by different researcher groups in recent years make it likely that high-resolution TOF-PET imaging with 100 ps time resolution can be demonstrated within the coming years. Reaching 10 ps would introduce a paradigm shift in PET imaging, allowing real time access to the dynamic of the image construction, one order of magnitude sensitivity increase and corresponding dose reduction. This could have positive consequences on the cost, as the same quantity of produced radioelements could serve more patients and/or be distributed to a larger perimeter. However, in order to reach the 10 ps range radically new approaches must be devised and investigated for the scintillator light generation, light transport, and light conversion.

This paper demonstrates that, not only there are no showstopper nor physical limits on any of these points, but that a number of enabling technologies open the route toward this very challenging goal. However, the integration of these technologies in complex multichannel systems without compromising the overall performance remains a very important issue that should not be neglected.

Moreover, new data processing and image reconstruction algorithms are required to optimally exploit the additional information acquired with such systems.

ACKNOWLEDGMENT

REFERENCES

[1] T. Jones and D. Townsend, "History and future technical innovation in positron emission tomography," *J. Med. Imag.*, vol. 4, no. 1, Jan./Mar. 2017, Art. no. 011013.

[2] P. A. Andersen *et al.*, "Radiation exposure to surgical staff during F-18-FDG-guided cancer surgery," *Eur. J. Nucl. Med. Mol. Imag.*, vol. 35, no. 3, pp. 624–629, 2008, doi: 10.1007/s00259-007-0532-0.

[3] (Sep. 2015). *The EXPLORER Project*. [Online]. Available: http://explorer.ucdavis.edu

[4] S. R. Cherry *et al.*, "Total-body imaging: Transforming the role of positron emission tomography," *Sci. Transl. Med.*, vol. 9, no. 381, Mar. 2017, Art. no. eaaf6169.

[5] D. F. C. Hsu *et al.*, "Studies of a next-generation silicon-photomultiplier-based time-of-flight PET/CT system," *J. Nucl. Med.*, vol. 58, no. 9, pp. 1511–1518, Sep. 2017, doi: 10.2967/jnumed.117.189514.

[6] B. Frisch, "Combining endoscopic ultrasound with Time-of-Flight PET: The EndoTOFPET-U.S. project," *Nucl. Instrum. Methods Phys. Res. A Accelerators Spectrometers Detectors Assoc. Equipment*, vol. 732, pp. 577–580, Dec. 2013.

[7] ERAMMIT Proposal, EU Horizon2020 INFRA-IA2 Call for Projects 2017.

[8] S. Gundacker *et al.*, "State of the art timing in TOF-PET detectors with LuAG, GAGG and L(Y)SO scintillators of various sizes coupled to FBK-SiPMs," *J. Instrum.*, vol. 11, no. 8, 2016, Art. no. P08008.

[9] R. F. Post and L. I. Schiff, "Statistical limitations on the resolving time of a scintillation counter" *Phys. Rev.*, vol. 80, no. 6, p. 1113, 1950.

[10] L. G. Hyman, R. M. Schwarcz, and R. A. Schluter, "Study of high speed photomultiplier systems," *Rev. Sci. Instrum.*, vol. 35, no. 3, pp. 393–406, 1964.

[11] S. Seifert, H. T. van Dam, and D. R. Schaart, "The lower bound on the timing resolution of scintillation detectors," *Phys. Med. Biol.*, vol. 57, no. 7, pp. 1797–1814, 2012.

[12] S. Gundacker *et al.*, "Time of flight positron emission tomography towards 100ps resolution with L(Y)SO: An experimental and theoretical analysis," *J. Instrum.*, vol. 8, no. 7, 2013, Art. no. P07014.

[13] F.-X. Gentit, "Litrani: A general purpose Monte-Carlo program simulating light propagation in isotropic or anisotropic media," *Nucl. Instrum. Methods Phys. Res. A Accelerators Spectrometers Detectors Assoc. Equipment*, vol. 486, nos. 1–2, pp. 35–39, Jun. 2002.

[14] S. Gundacker, E. Auffray, K. Pauwels, and P. Lecoq, "Measurement of intrinsic rise times for various L(Y)SO and LuAG scintillators with a general study of prompt photons to achieve 10 ps in TOF-PET," *Phys. Med. Biol.*, vol. 61, no. 7, pp. 2802–2837, 2016.

[15] A. Vasiliev, "Relaxation of hot electronic excitations in scintillators: Account for scattering, track effects, complicated electronic structure," in *Proc. 5th Int. Conf. Inorganic Scintillators Appl. (SCINT)*, 1999, pp. 43–52.

[16] P. Lecoq, M. Korzhik, and A. Vasiliev, "Can transient phenomena help improving time resolution in scintillators?" *IEEE Trans. Nucl. Sci.*, vol. 61, no. 1, pp. 229–234, Feb. 2014.

[17] S. Gundacker *et al.*, "State of the art timing in TOF-PET detectors with LuAG, GAGG and L(Y)SO scintillators of various sizes coupled to FBK-SiPMs," *J. Instrum.*, vol. 11, no. 8, 2016, Art. no. P08008.

[18] D. I. Vaisburd, P. A. Palyanov, B. N. Semin, and O. M. Shumskiy, "Simultaneous observation of intraband electron and interband hole radioluminescence for CsI crystals," *Rep. USSR Acad. Sci.*, vol. 336, pp. 39–42, 1994.

[19] S. I. Omelkov, V. Nagirnyi, A. N. Vasil̂ev, and M. Kirm, "New features of hot intraband luminescence for fast timing," *J. Luminescence*, vol. 176, pp. 309–317, Aug. 2016.

[20] W. Lehmann, "Edge emission of n-type conducting ZnO and CdS," *Solid State Electron.*, vol. 9, nos. 11–12, pp. 1107–1110, 1966.

[21] S. Derenzo, M. J. Weber, and M. K. Klintenberg, "Temperature dependence of the fast, near-band-edge scintillation from CuI, HgI2, PbI2, ZnO:Ga and CdS:In," *Nucl. Instrum. Methods Phys. Res. A Accelerators Spectrometers Detectors Assoc. Equipment*, vol. 486, pp. 214–219, Jun. 2002.

[22] H. Buresova *et al.*, "Preparation and luminescence properties of ZnO:Ga—Polystyrène composite scintillator," *Opt. Exp.*, vol. 24, no. 14, Art. no. 15289, Jul. 2016.

[23] J. Q. Grim *et al.*, "Continuous-wave biexciton lasing at room temperature using solution-processed quantum wells," *Nat. Nanotechnol.*, vol. 9, pp. 891–895, Oct. 2014.

[24] R. M. Turtos *et al.*, "Ultrafast emission from colloïdal nanocrystals under pulsed X-ray excitation,"*J. Instrum.*, vol. 11, Oct. 2016, Art. no. P10015.

[25] P. Lecoq, "Metamaterials for novel X- or γ-ray detector designs," in *Proc. IEEE Nucl. Sci. Symp. Conf. Rec.*, Dresden, Germany, 2008, pp. 680–684.

[26] S. Gundacker *et al.*, "Time resolution deterioration with increasing crystal length in a TOF-PET system," *Nucl. Instrum. Methods Phys. Res. A Accelerators Spectrometers Detectors Assoc. Equipment*, vol. 737, pp. 92–100, Feb. 2014.

[27] M. Kronberger, E. Auffray, and P. Lecoq, "Probing the concepts of photonic crystals on scintillating materials," *IEEE Trans. Nucl. Sci.*, vol. 55, no. 3, pp. 1102–1106, Jun. 2008.

[28] E. Yablonovitch, "Inhibited spontaneous emission in solid-state physics and electronics," *Phys. Rev. Lett.*, vol. 58, no. 20, pp. 2059–2062, 1987.

[29] S. John, "Strong localization of photons in certain disordered dielectric superlattices," *Phys. Rev. Lett.*, vol. 58, no. 23, pp. 2486–2489, 1987.

[30] B. Singh *et al.*, "Enhanced scintillation light extraction using nanoimprinted photonic crystals," *IEEE Trans. Nucl. Sci.*, to be published.

[31] A. Knapitsch and P. Lecoq, "Review on photonic crystal coatings for scintillators," *Int. J. Modern Phys. A*, vol. 29, no. 30, 2014, Art. no. 1430070.

[32] M. V. Nemallapudi, S. Gundacker, P. Lecoq, and E. Auffray, "Single photon time resolution of state of the art SiPMs," *J. Instrum.*, vol. 11, Oct. 2016, Art. no. P10016.

[33] S. Mandai and E. Charbon, "Multi-channel digital SiPMs: Concept, analysis and implementation," in *Proc. IEEE Nucl. Sci. Symp. Conf. Rec.*, Anaheim, CA, USA, 2012, pp. 1840–1844.

[34] T. Frach *et al.*, "The digital silicon photomultiplier—Principle of operation and intrinsic detector performance," in *Proc. IEEE Nucl. Sci. Symp. Conf. Rec.*, Orlando, FL, USA, 2009, pp. 1959–1965.

[35] S. Gundacker, E. Auffray, P. Jarron, T. Meyer, and P. Lecoq, "On the comparison of analog and digital SiPM readout in terms of expected timing performance," *Nucl. Instrum. Methods Phys. Res. A Accelerators Spectrometers Detectors Assoc. Equipment*, vol. 787, pp. 6–11, Jul. 2015.

[36] K. Doroud and M. C. S. Williams, "A new approach for improved time and position measurements for TOF-PET: Time-stamping of the photoelectrons using analogue SiPMs," *Nucl. Instrum. Methods Phys. Res. A Accelerators Spectrometers Detectors Assoc. Equipment*, vol. 849, pp. 16–19, Mar. 2017.